Biomaterials Science

ROYAL SOCIETY OF CHEMISTRY

PAPER

View Article Online
View Journal | View Issue

Cite this: *Biomater. Sci.*, 2024, **12**, 1211

Wound microenvironment regulatory poly(L-glutamic acid) composite hydrogels containing metal ion-coordinated nanoparticles for effective hemostasis and wound healing†

Yanzheng Chen,[a] Xueliang Zhang,[a] Qing Wang,[d] Chang Du*[b,c] and Chang-Ming Dong *[a]

Regulating the wound microenvironment to promote proliferation, vascularization, and wound healing is challenging for hemostats and wound dressings. Herein, polypeptide composite hydrogels have been simply fabricated by mixing a smaller amount of metal ion-coordinated nanoparticles into dopamine-modified poly(L-glutamic acid) (PGA), which had a microporous size of 10–16 μm, photothermal conversion ability, good biocompatibility, and multiple biological activities. *In vitro* scratch healing of fibroblast L929 cells and the tube formation of HUVECs provide evidence that the PGA composite hydrogels could promote cell proliferation, migration, and angiogenesis with the assistance of mild photothermia. Moreover, these composite hydrogels plus mild photothermia could effectively eliminate reactive oxygen species (ROS), alleviate inflammation, and polarize the pro-inflammatory M1 macrophage phenotype into the pro-healing M2 phenotype to accelerate wound healing, as assessed by means of fluorescent microscopy, flow cytometry, and quantitative real-time polymerase chain reaction (qRT-PCR). Meanwhile, a rat liver bleeding model illustrates that the composite hydrogels reduced the blood loss ratio to about 10% and shortened the hemostasis time to about 25 s better than commercial chitosan-based hemostats. Furthermore, the full-thickness rat skin defect models showcase that the composite hydrogels plus mild photothermia could proheal wounds completely with a fast healing rate, optimal neovascularization, and collagen deposition. Therefore, the biodegradable polypeptide PGA composite hydrogels are promising as potent wound hemostats and dressings.

Received 4th December 2023,
Accepted 28th December 2023

DOI: 10.1039/d3bm01978k

rsc.li/biomaterials-science

1 Introduction

Wound healing is a complex process in surgical management,[1] and excessive reactive oxygen species (ROS), inflammation, immune imbalance, and obstruction of neovascularization are common phenomena in wounds. These factors interact with each other and form negative feedback loops to delay wound healing.[2,3] In particular, adjusting the inflammation and increasing neovascularization are crucial during the wound healing process.[4,5] Macrophages in wounds are key immune cells with heterogeneous plasticity for regulating the immune microenvironment.[6] It is generally believed that classically activated macrophages (*i.e.*, pro-inflammatory phenotype M1) and alternatively activated macrophages (*i.e.*, anti-inflammatory and pro-healing phenotype M2) are two typical phenotypes to regulate immunity in wounds. The M1 phenotype releases pro-inflammatory cytokines such as tumor necrosis factor-α (TNF-α), while the M2 phenotype mediates anti-inflammatory responses to promote proliferation and angiogenesis. The ineffective transformation of macrophages from M1 to M2 would lead to sustained inflammation and delayed wound healing. Therefore, the construction of macrophage-polarizing materials becomes a promising wound microenvironment regulatory method.

On the other hand, physical regulation, including temperature regulation, is a simple means of controlling the wound

[a]*School of Chemistry and Chemical Engineering, Shanghai Jiao Tong University, Shanghai 200240, P. R. China. E-mail: cmdong@sjtu.edu.cn*
[b]*Clinical Cancer Institute, Center for Translational Medicine, Naval Military Medical University, Shanghai, 200433, P. R. China. E-mail: cdu@shsci.org*
[c]*State Key Laboratory of Systems Medicine for Cancer, Shanghai Cancer Institute, Ren Ji Hospital, School of Medicine, Shanghai Jiao Tong University, Shanghai, 200240, P. R. China*
[d]*Department of Stomatology, Shanghai General Hospital, Shanghai Jiao Tong University, Shanghai, 200080, P. R. China*

†Electronic supplementary information (ESI) available: Materials, methods, Tables S1–S3, and Fig. S1–S16. See DOI: https://doi.org/10.1039/d3bm01978k

microenvironment, as hyperthermia has been used in clinical cancer treatments. Cell proliferation and metabolism slow down, along with hindered collagen deposition, when the temperature of wounds drops below 33 °C, thereby delaying wound healing.[7,8] Therefore, near-infrared radiation (NIR)-mediated hyperthermia has been proven to assist wound healing in addition to tumor and infection treatments.[9,10] Considering that a high temperature kills cells (>43 °C), a mild temperature around 40–42 °C is reported to promote angiogenesis and endothelial cell tube formation, becoming a simple method to assist wound healing.[11]

Owing to their excellent biocompatibility, tunable softness, elasticity mimicking the extracellular matrix (ECM), 3D networks for absorbing wound exudates, and even designable bioactivities, polymeric hydrogels are considered competitive candidates for wound dressings.[12–14] Among them, polypeptides are polymerized from natural amino acid-based monomers with good biocompatibility, biodegradability, and chemical diversity,[15] enabling them to be a promising platform for biomedical hydrogels and dressings.[16] For example, two-component polypeptide hydrogels have been facilely prepared through *o*-phthalaldehyde-terminated four-arm poly (ethylene glycol) and ε-polylysine, showing adjustable mechanical and degradation properties to close wounds and promote wound healing.[17] In contrast to polylysine, with some positive charges causing cell membrane damage in physiological media, PGA with negative charges has better biocompatibility. As a typical polypeptide with easy synthesis and a potential transition, we found that the dopamine-modified PGA could form a lower concentrated hydrogel (1 wt%) with excellent biocompatibility to accelerate wound healing.[18] However, constructing polypeptide hydrogels with wound environment-modulating capabilities is still challenging for high-performance wound dressings.

To address the above-mentioned challenges, including inflammation and immune regulation in wound healing, we constructed a novel type of dopamine-modified PGA composite hydrogel containing metal ion-coordinated nanoparticles, which integrates controllable NIR-mediated hyperthermia and metal ions to regulate inflammation and macrophage polarization functions for highly effective wound healing management (Scheme 1). *In vitro* and *in vivo* assays showcase that the PGA composite hydrogels could synergistically promote cell proliferation, migration, and neovascularization upon mild hyperthermia stimulation. Remarkably, these composite hydrogels containing 0.1 wt% metal-ions@tannic acid (TA) nanoparticles effectively alleviated inflammation and transformed the pro-inflammatory M1 macrophage phenotype to differentiate into the pro-healing M2 phenotype. These factors were orchestrated to promote optimal neovascularization and collagen deposition, resulting in fast and high-performance healing as assessed by full-thickness skin defect wounds in rats and various immunohistological and immunofluorescent assays. Therefore, this work provides a simple method to construct polypeptide PGA composite hydrogels that can effectively regulate the wound microenvironment for wound dressings.

2 Results and discussion

2.1 Preparation and physical characterization of the PGA composite hydrogels

Biocompatible metal ions (*e.g.*, Zn^{2+} and Fe^{2+}) are abundant and play important regulatory roles in life activities. Fe^{2+} can promote angiogenesis for wound healing;[11] on the other hand, as a catalytic cofactor, Zn^{2+} regulates oxidative stress and immunity.[19] Considering the multiple biological functions of Fe^{2+} and Zn^{2+}, the ROS clearance activity of natural multiphenols (TA) as metal ligands,[20,21] and the easy preparation and good biocompatibility of dopamine-modified PGA (Fig. S1–S5 and Table S1, ESI†), injectable PGA composite hydrogels were simply constructed by mixing 0.1 wt% metal ion-coordinated nanoparticles (Zn^{2+}@TA, Fe^{2+}@TA, Fe^{2+}-Zn^{2+}@TA) into 1 wt% dopamine-modified PGA hydrogels according to our previous work.[18] Owing to multiple hydrogen-bonding interactions among the TA-coated nanoparticles and the PGA network, the composite quickly gelled at room temperature within about 30 s, enabling the composite hydrogels to seal wounds.[22] Meanwhile, the PGA composite hydrogels were easily injected into the shape of a "star" and the letters "SJTU," which adhered to pig skin and could be physically removed from the skin under the flushing of water flow (Fig. S6†). These injectability, skin adherence, and detachment properties have clinical implications for those composite hydrogels to fill irregular wounds and detach for further medical management.

The ECM of skin tissue is a porous 3D network that supports cell growth and guides tissue regeneration, and the pore size is a key factor affecting cell adhesion, migration, and proliferation.[23] So, the microporous structure is evaluated for those hydrogels as wound dressings. As shown in Fig. 1a, scanning electron microscopy (SEM) was used to observe the microstructure, and the lyophilized hydrogels had a densely interconnected porous microstructure with a pore size of about 10–16 μm (Fig. S7†). Specifically, the average pore size of the H-Fe^{2+}-Zn^{2+} and H-Zn^{2+} cryogels was, respectively, 12.6 ± 4.0 μm and 15.5 ± 5.6 μm, higher than that of pure H (11.4 ± 3.4 μm). In addition, the swelling test also showed that the microporous network could quickly absorb water in 1 h with a swelling ratio of about 1250% and remained nearly constant for 12 h compared to the pure H network, suggesting the composite networks were more stable than their pure counterparts (Fig. S8†). As a note, subsequent hemostasis and healing experiments also showed that the PGA composite hydrogels could rapidly absorb blood and exudate to maintain a moist healing environment in the following studies. In addition, the hydrogels of H, H-Fe^{2+}, H-Zn^{2+}, and H-Fe^{2+}-Zn^{2+} were characterized by a rheometer to investigate their rheological behavior and mechanical properties. As shown in Fig. 1b, the frequency-sweep spectra show that the storage modulus (G') was consistently higher than the loss modulus (G'') over a frequency range of 0.1 to 100 rad per s, confirming the typical elastic mechanical behavior of the hydrogels. Apparently, a smaller amount of 0.1 wt% metal-ions@TA nanoparticles in

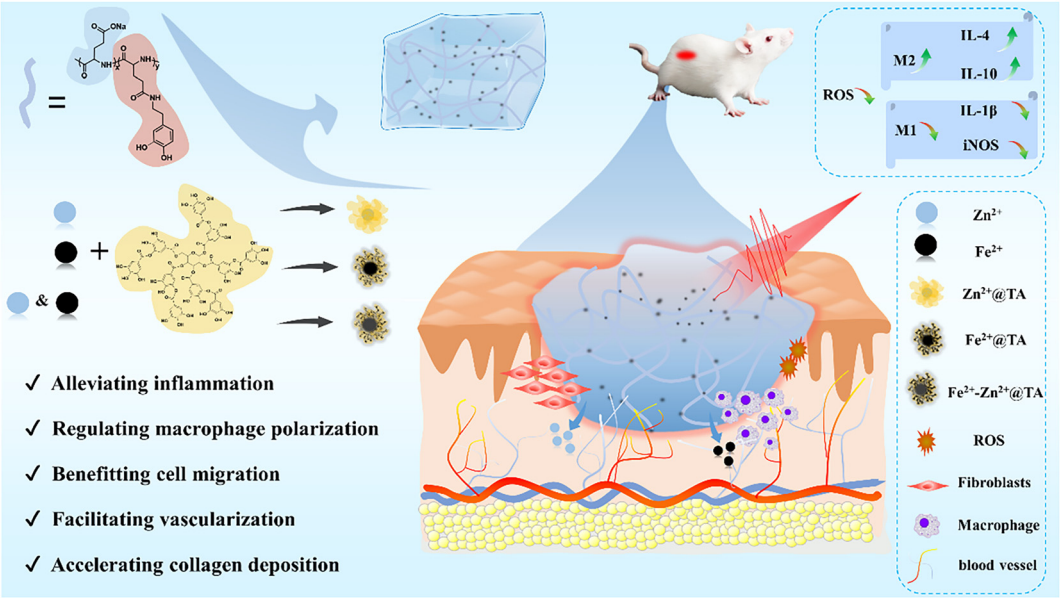

Scheme 1 Schematic diagram for the preparation of the PGA composite hydrogels to regulate the wound microenvironment, including inflammation and macrophage polarization, for wound healing.

the composite hydrogels enhanced the mechanical storage modulus by about 4–6 times compared to pure H, which might be due to the π–π stacking and hydrogen-bonding interactions among the dopamine-modified PGA network with polyphenolic TA-coated nanoparticles.[24,25]

2.2 Antioxidant and photothermal properties of the PGA composite hydrogels

ROS are concomitantly produced during the inflammation period of wounds, while excess ROS would inhibit wound healing in the later stage. 1,1-Diphenyl-2-picrylhydrazine (DPPH$^{\bullet}$) was used to evaluate the antioxidant capacity of hydrogels by testing characteristic absorption at 517 nm.[26] As shown in Fig. 1c, the PGA composite hydrogels showed significant decolorization compared to the control group, indicating that they have good DPPH clearance ability. Fig. 1d indicates that the composite hydrogels presented a higher radical clearance ratio of over 83% compared to pure H, with a clearance ratio of about 45%. This demonstrates that the PGA composite hydrogels have excellent antioxidant activities to clear ROS for wound pro-healing.[27]

NIR-mediated mild photothermia holds potential for wound management.[28] As shown in Fig. 1e and f, the composite hydrogels of H-Fe^{2+} and H-Fe^{2+}-Zn^{2+}, respectively, increased the temperature by a ΔT of 20.0 °C and 15.7 °C faster than pure H (4.5 °C) when irradiated for 10 min by an 808 nm laser at 1 W cm^{-2}; this is because the added metal-ions@TA have a good photothermal conversion ability. The ΔT of H-Fe^{2+} did not change after three heating–cooling cycles, proving good photothermal stability (Fig. 1g). Meanwhile, H-Fe^{2+} and H-Fe^{2+}-Zn^{2+} exhibited concentration-dependent heat generation under NIR irradiation (Fig. 1h), which was used for temperature control in subsequent animal experiments. Based on the above results and considering that high temperatures would burn normal skin surrounding wounds, the photothermal amplitude can be adjusted by adding the percentage of metal-ions@TA nanoparticles for effective wound management.[29]

2.3 *In vitro* and *in vivo* biocompatibility of the PGA composite hydrogels

Good biocompatibility is a prerequisite for the performance of wound dressings. First, the proliferation activity of L929 cells on hydrogels was measured by means of live/dead cell double staining (Fig. S9†) and the common MTT method. As shown in Fig. 2a, the composite hydrogels of Zn^{2+}@TA and Fe^{2+}-Zn^{2+}@TA gave relatively greater OD values than Fe^{2+}@TA and pure H, probably because Zn^{2+} could enhance cell proliferation.[30,31] In particular, upon NIR irradiation (10 min, 808 nm, 1 W cm^{-2}), H-Fe^{2+}-Zn^{2+}-NIR and H-Fe^{2+}-NIR achieved a higher OD than those without NIR irradiation, showcasing mild photothermal stimulation on cell proliferation.[11] Moreover, the hydrogel dressing would directly contact damaged tissues, and the blood compatibility was characterized by an *in vitro* hemolysis experiment. The hemolysis ratio of all hydrogels is below 1% and far below the common standard of 5% (Fig. 2b and c), and the composite hydrogels showed no difference with pure H and PBS. These results indicate that the PGA composite hydrogels have excellent blood compatibility. This is attributed to the fact that PGA with a negatively charged backbone would not cause destruction on the cell membrane, thus inducing lower hemolysis.

To determine whether the hydrogels would degrade without residual toxicity or induce inflammation that affects wound

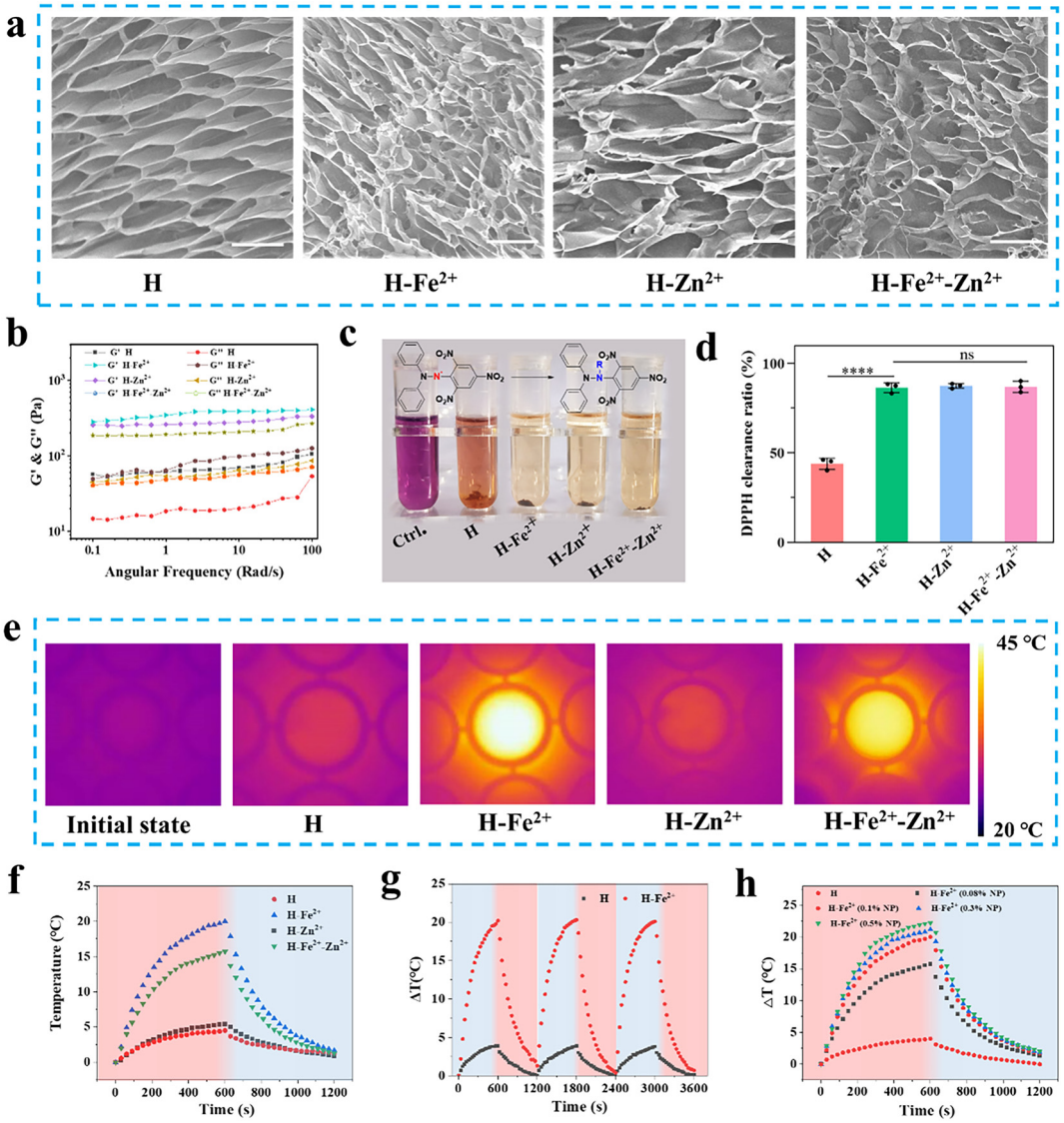

Fig. 1 Physical and photothermal characterizations of the PGA composite hydrogels. (a) Representative SEM for cryogels (scale bar = 30 μm); (b) rheological curves; (c) representative digital photos for DPPH measurement; and (d) the clearance ratio (n = 3, ****p < 0.0001); (e) representative photothermal images taken by an infrared camera; (f) photothermal curves; (g) photothermal stability; and (h) those of H-Fe^{2+} with different contents of Fe^{2+}@TA.

healing, *in vivo* histocompatibility was assessed by subcutaneous hydrogel implantation and an H&E immunohistological assay (Fig. 2d). The tissues near subcutaneous hydrogel-implanted sites retained skin integrity for H-Zn^{2+} and H-Fe^{2+}-Zn^{2+}, and no bleeding, edema, or necrosis was observed on day 14. Note that H-Zn^{2+} and H-Fe^{2+}-Zn^{2+} showed weaker inflammation than H-Fe^{2+} and pure H because Zn^{2+} could induce proinflammatory M1 macrophages into pro-healing M2 macrophages, thereby reducing the inflammation response, as further studied in the following.[30] Fig. 2e shows that the hydrogels degraded to about 33–44 wt% on day 7 and then to about 13–29 wt% on day 14, and the composite hydrogels degraded faster than pure H, which was probably due to their large pores enabling them to swell and metal-ions@TA nanoparticles recruiting macrophages for digestion, as studied in the following.[32,33] These data provide evidence that the PGA composite hydrogels have good biocompatibility *in vivo*, which is consistent with the above cell viability and hemolysis *in vitro*.

2.4 *In vitro* cell migration and angiogenesis

The interaction between cells and materials is crucial in wound healing, which manifests in promoting cell migration, regulating inflammatory cell differentiation, and enhancing angiogenesis.[34] The effects of hydrogels and mild photothermal stimulation on cell migration were evaluated by a series of scratch tests. To ensure that cell migration is not caused by cell proliferation, L929 cells were respectively starved with low

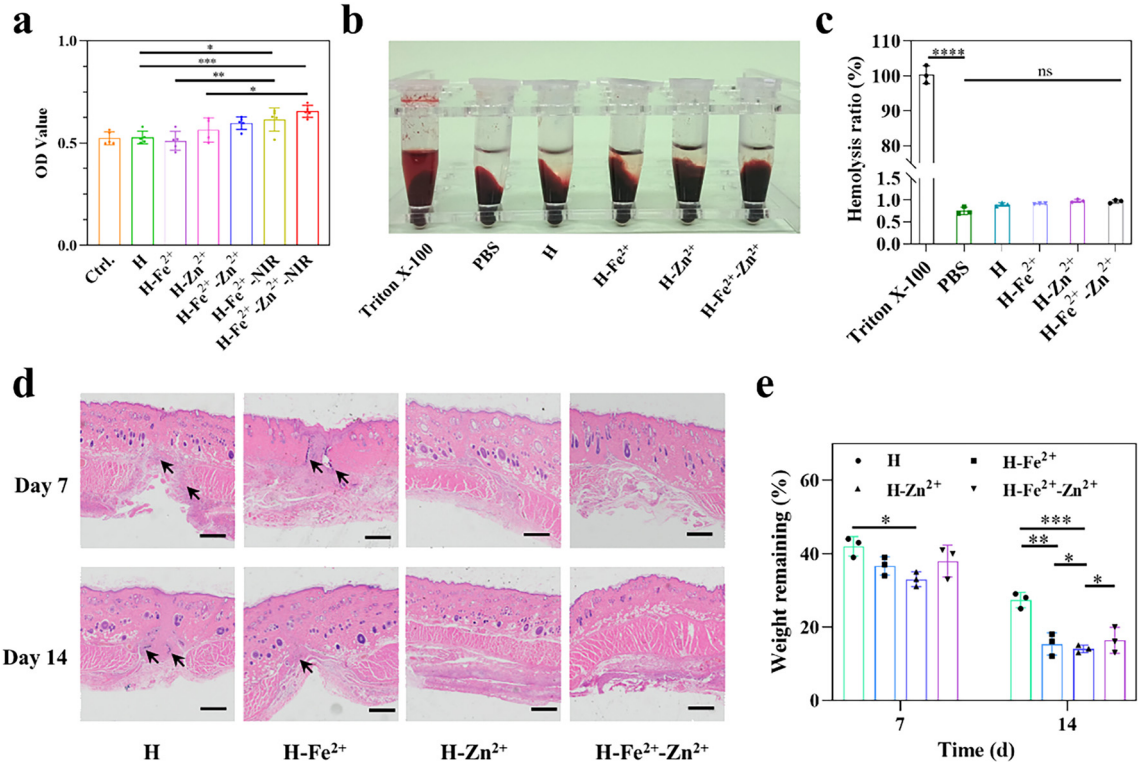

Fig. 2 Biocompatibility evaluation of the PGA composite hydrogels. (a) The proliferation activity of L929 cells; (b) representative digital photos of hemolysis experiments; (c) hemolysis ratio; (d) representative H&E staining images of the skins near subcutaneous implantation (scale bar = 500 μm; the black arrow points towards inflammatory cells); and (e) weight remaining *in vivo* (n = 3, *p < 0.05, **p < 0.01, ***p < 0.001, ****p < 0.0001).

serum-containing culture medium for 24 h before construction of the scratch according to a previous protocol.[35] The cell migration status was recorded at a pre-set time, followed by analysis of the images by measuring the area between the forefronts of migrating cells on both sides. As shown in Fig. 3a and c, the H-Fe^{2+}-Zn^{2+}-NIR group exhibited complete scratch closure with a maximum migration at 48 h compared with the others, and the scratch healing rate was in the order of the composite hydrogel + NIR > the composite hydrogel > pure H hydrogel, indicating both mild photothermal stimulation and metal ions cooperatively promoted cell migration.[36]

Early microvascular regeneration and vascular network reconstruction are crucial for the healing of full-thickness skin defects.[37] Therefore, the angiogenesis activity of hydrogels was evaluated by the *in vitro* endothelial tube formation of HUVECs (Fig. 3b). Semi-quantitative analyses on the node number (Fig. 3d) and total capillary length (Fig. 3e) were used to validate the results with Image J software.[38] The HUVECs co-incubated with the composite hydrogels showed highly enhanced activity in new blood vessel formation compared with pure H, and H-Fe^{2+}-Zn^{2+} and H-Zn^{2+} outperformed H-Fe^{2+}. These data indicate that both Zn^{2+}@TA and Fe^{2+}@TA can promote angiogenesis, which is consistent with the above cell migration.[39] Significantly, there is a big increase in angiogenesis when comparing H-Fe^{2+}-Zn^{2+}+NIR and H-Fe^{2+}-NIR with no-NIR-exposed groups, showing that mild photothermal stimulation could highly promote the angiogenesis of HUVECs *in vitro*, which is similar to previous reports stating that mild hyperthermia upregulated the expression of vascular endothelial growth factor (VEGF) and promoted the growth of new blood vessels.[40] Overall, the tube formation assay demonstrates that both Zn^{2+}@TA and Fe^{2+}@TA and mild photothermia can synergistically promote the proliferation and tubular formation of HUVECs, which is in agreement with the above cell migration.

Moderate inflammation in wounds is pro-healing in the initial stage, but excessive ROS affects the proliferation of fibroblasts and the differentiation of macrophages, triggers heavy inflammation, and thus inhibits tissue regeneration.[41] Therefore, the ROS scavenging ability of the hydrogels incubated in L929 cells was evaluated using a 2,7-dichlorodihydrofluorescein diacetate (DCFH-DA) probe. DCFH-DA itself does not fluorescence and is hydrolyzed by some esterases to generate non-fluorescent DCFH, which is oxidized by ROS to produce fluorescent DCF. Thus, the level of intracellular ROS can be determined by detecting the fluorescence of DCF (Fig. S10†). As shown in Fig. 3f and g, the PBS group was observed to have scattered green colors, indicating the cells were in a normal state with a low ROS level; bright green fluorescence was displayed after incubation with 100 μM H_2O_2, indicating that H_2O_2 induced a massive production of ROS in L929 cells.[42] However, the fluorescence was heavily weakened by the PGA composite hydrogels compared with pure H hydrogel, indicating that plenty of ROS were removed, mainly due to

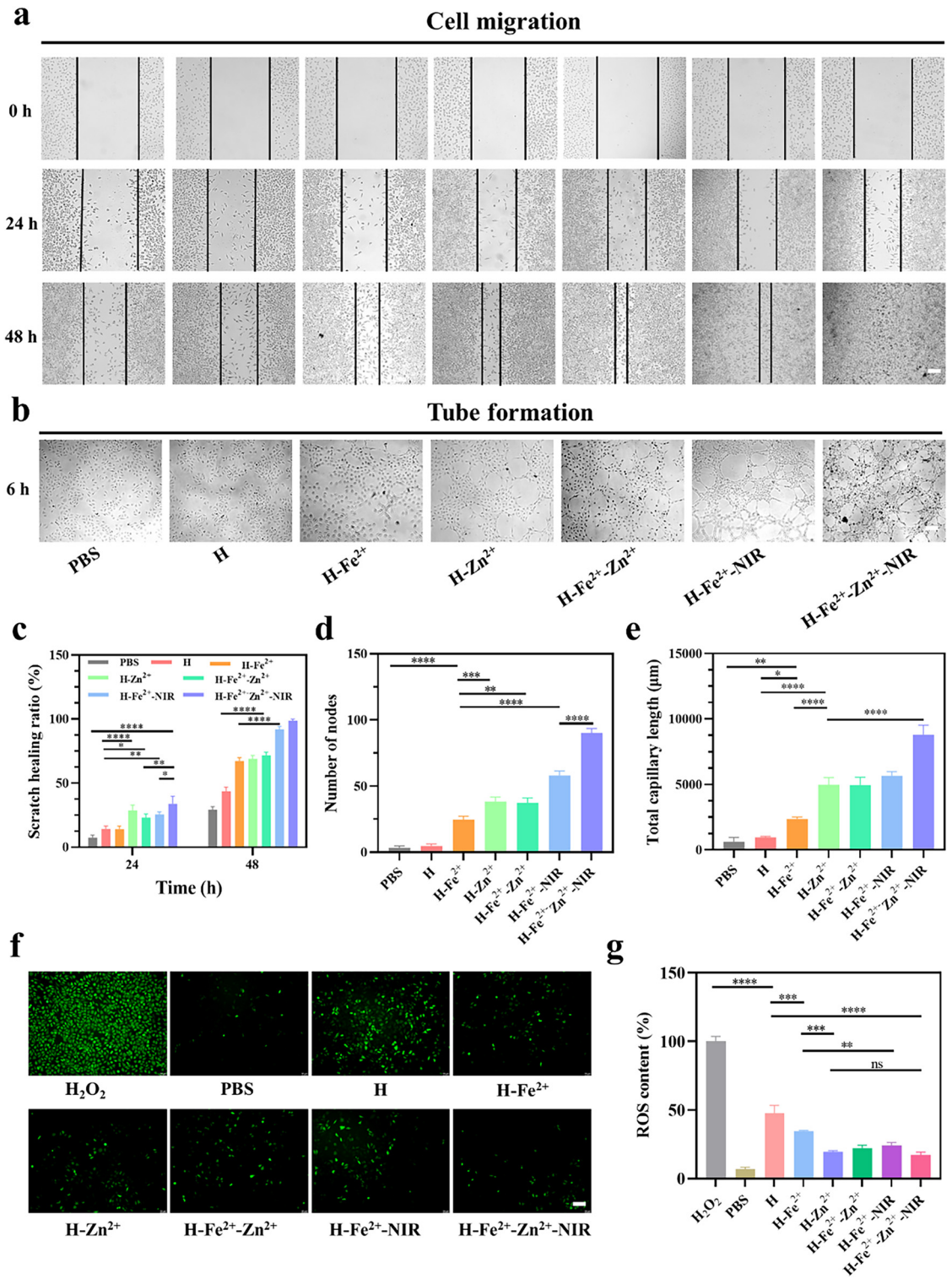

Fig. 3 Migration, angiogenesis, and ROS levels in cells when incubated on different hydrogels *in vitro*. (a) Representative photos for wound scratch healing of L929 (scale bar = 100 μm); (b) representative photos for the tube formation of HUVECs (scale bar = 100 μm); (c) scratch healing ratio of L929; (d) the number of nodes and (e) total capillary length of HUVECS; (f) representative fluorescence images (scale bar = 100 μm); and (g) ROS content in H_2O_2-stimulated L929 (n = 3, *p < 0.05, **p < 0.01, ***p < 0.001, ****p < 0.0001).

the scavenging ability of metal-ions@TA nanoparticles. Note that mild photothermia had a slight effect on the ROS clearance from L929 cells. Taken together, these results demonstrate the PGA composite hydrogels can effectively clear massive ROS levels in an inflammation-mimetic microenvironment *in vitro*.

2.5 *In vitro* macrophage polarization and transition from M1 to M2

Macrophages play an important role in multiple stages of inflammation regulation and tissue reconstruction during wound healing.[6] The pro-inflammatory M1 phenotype in wounds releases inflammatory cytokines to induce apoptosis and disrupt collagen deposition, while the pro-healing M2 phenotype can accelerate fibroblast proliferation, coordinate anti-inflammatory responses, and promote angiogenesis and ECM remodeling. The failure of macrophages to transition from M1 to M2 often leads to chronic wounds and even scar formation.[43,44] Using CD86 and CD206 as M1 and M2 biomarkers, CD86/CD206-labeled immunofluorescence staining was performed to confirm the regulatory actions of hydrogels on macrophages, during which macrophages were stimulated and then co-incubated with hydrogels.[45] Compared with the control groups of PBS, pure H and H + LPS (Fig. S11†), the composite hydrogels presented obviously weakened fluorescence, indicating that metal-ions@TA, to some extent, inhibited M1 due to the anti-inflammation of TA.[46] H-Zn^{2+} showed the greatest inhibitory effect on M1 polarization compared to H-Fe^{2+} and the others, while mild photothermia had less effect on the polarization, suggesting that Zn^{2+} ions played a major role in regulating the M2 polarization.[47,48] Meanwhile, the composite hydrogels had a reverse regulatory effect on the polarization of the pro-healing M2 phenotype. In all, the PGA composite hydrogels could polarize macrophages from pro-inflammatory M1 to pro-healing M2 due to the cooperative roles of metal ions and TA, as consistent with a previous study on metal ion-coordinated hydrogels.[49] Flow cytometry is further used to evaluate the macrophage phenotype.[50] Compared with H and PBS, the RAW 264.7 cells in H-Fe^{2+}-Zn^{2+}, H-Fe^{2+}-Zn^{2+}-NIR, and H-Zn^{2+} had a progressive tendency to upregulate CD206, ranging from 14.7% to 18.7%, until 19.2% (Fig. 4a, b and Fig. S12†). All results provide evidence that H-Zn^{2+}, H-Fe^{2+}-Zn^{2+}, and H-Fe^{2+}-Zn^{2+}-NIR could effectively polarize macrophages from M1 to M2, which would enhance the synthesis of the extracellular matrix in fibroblasts, promote endothelial cell angiogenesis, and thus promote tissue regeneration.[51]

M1 typically secretes high levels of nitric oxide synthase (iNOS) and the inflammatory cytokine interleukin IL-1β, while M2 produces anti-inflammatory cytokines such as IL-4 and IL-10. Therefore, a quantitative real-time polymerase chain reaction (qRT-PCR) was used to evaluate hydrogels regulating the expression of inflammation-related genes. Fig. 4c–f show that the H-Zn^{2+} hydrogel had the most prominent ability to downregulate inflammation-related genes and upregulate anti-inflammatory-related genes compared to H-Fe^{2+} and the others. In addition, both H-Fe^{2+}-NIR and H-Fe^{2+}-Zn^{2+}-NIR showed slight downregulation of inflammation-related genes and upregulation of anti-inflammatory-related genes compared with non-NIR-exposed groups. Collectively, the above results of CD86/CD206 labeled immunofluorescence, flow cytometry, and qRT-PCR convincingly demonstrate that the PGA composite hydrogels could modulate the macrophages from pro-inflammatory M1 to pro-healing M2, and H-Zn^{2+} outperformed H-Fe^{2+} and H-Fe^{2+}-Zn^{2+}, while mild photothermal stimulation had a slight effect. These merits enable the hydrogels to shorten inflammatory duration and further promote wound healing, as studied in the following.

2.6 *In vitro* and *in vivo* hemostatic properties

Hemostasis is an initial step in the wound healing process,[1,52] and the hemostasis properties were evaluated by measuring the *in vitro* blood coagulation index (BCI) and the adhesion of red blood cells (RBC), as shown in Fig. 5a and b. The lower BCI index and the higher adhesion ratio of RBC indicate better hemostatic properties. Compared with pure H, the composite hydrogels gave lower BCI values and a higher adhesion ratio of RBC, indicating that they had a faster blood coagulation rate, while the metal ions of Fe^{2+} and Zn^{2+} have no obvious difference on the blood clotting. This is because the composite hydrogels have a relatively larger pore size to absorb blood, and the metal ions would activate platelets to promote blood clotting.[33,53] *In vivo* hemostasis was further verified by a rat liver bleeding model (Fig. 5c). As shown in Fig. 5d–f and Fig. S13,† H-Zn^{2+}, H-Fe^{2+}, and H-Fe^{2+}-Zn^{2+} significantly shortened the hemostasis time to about 25 s compared to about 60 s for H and commercial chitosan-based hydrogel hemostats and reduced the blood loss ratio to about 10% compared to about 18% for H and 61% of the chitosan-based hydrogel hemostat. The excellent hemostasis can be attributed to the fact that the composite hydrogels had rapid swelling properties (Fig. S8†) and a suitable microporous structure to absorb blood and confine red blood cells, and might activate platelets *via* the procoagulant effect of Zn^{2+} or Fe^{2+}.[33,53] Therefore, the PGA composite hydrogels possess excellent hemostatic properties useful for wound sealants and hemostats.

2.7 *In vivo* wound healing performance of the hydrogels

The full-thickness skin defect model had circular wounds with a diameter of 10 mm on the back of healthy Sprague Dawley (SD) rats, which were used to evaluate wound healing *in vivo* when the hydrogels were immediately treated at prescribed times (Fig. 6a). H-Fe^{2+}-NIR and H-Zn^{2+}-Fe^{2+}-NIR represent the treatment subjected to the NIR irradiation (10 min, 808 nm, 1 W cm^{-2}, twice a day) on days 0, 1, and 2, respectively (Fig. 6b), and an infrared camera was used to record the temperature change at the wounds (Fig. S14†). The temperature at the wounds fluctuated between 40 and 42 °C, which is below the threshold of 43 °C that would kill cells.[54] On day 3, the wound areas in all hydrogels were smaller than those in the control groups of blank PBS and Tegaderm, indicating that the hydrogel dressing was conducive to wound contraction (Fig. 6c and d). On the 7th day, the wounds significantly reduced to less than 25.0% for those composite hydrogels with/without NIR stimulation; however, the wounds in PBS and Tegaderm remained as high as 60.5% and 40.0%, respectively. Remarkably, the wounds in H-Fe^{2+}-Zn^{2+} and H-Fe^{2+}-Zn^{2+}-NIR fully healed on the 12th day, while those in H-Zn^{2+} and H-Fe^{2+}-

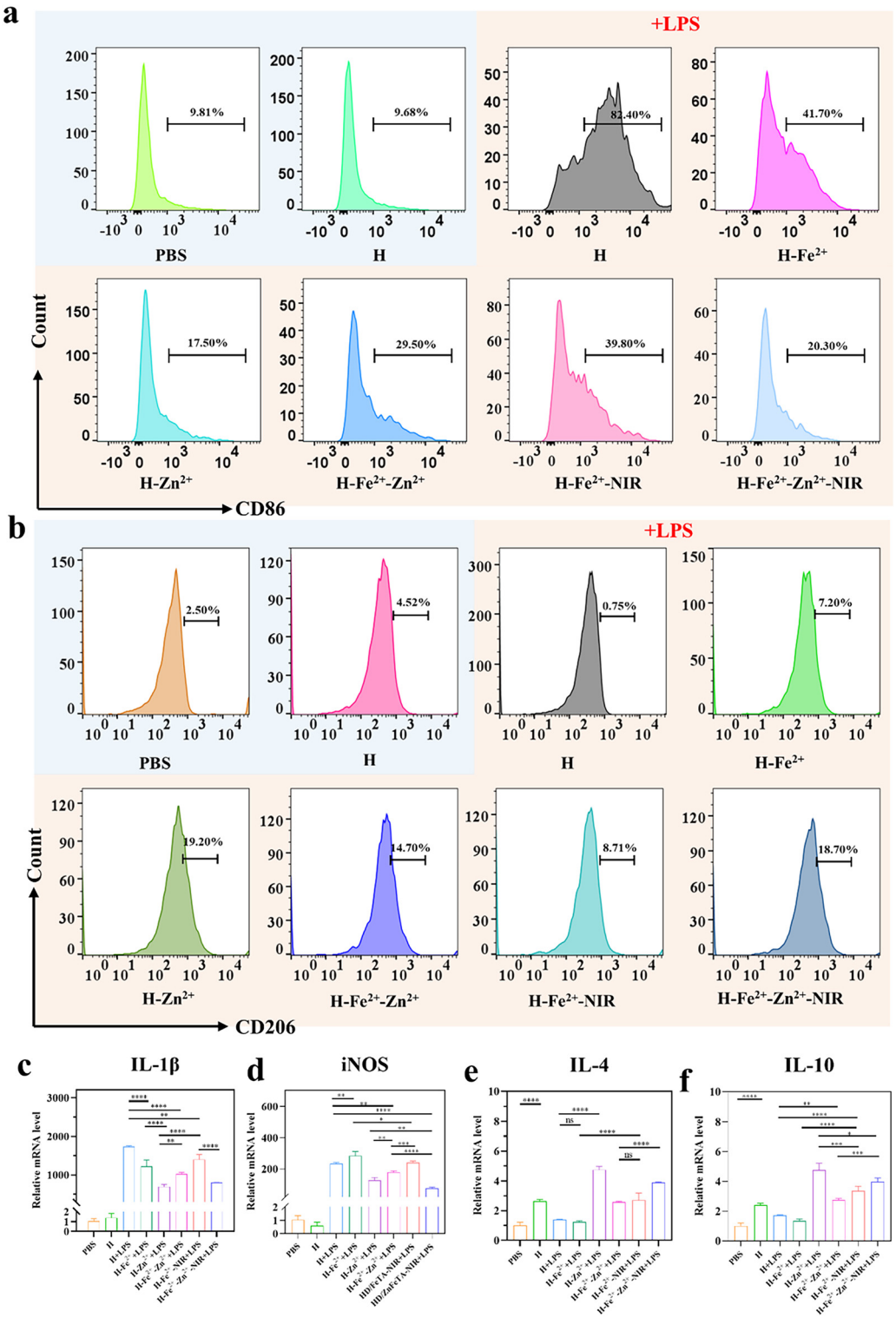

Fig. 4 *In vitro* macrophage polarization of RAW 264.7. Flow cytometry plots showing the presence of (a) M1 [CD86+] and (b) M2 [CD206+] macrophages; inflammation-related gene expression of (c) IL-1β, (d) iNOS, (e) IL-4, and (f) IL-10 determined by a quantitative real-time polymerase chain reaction (qRT-PCR) (n = 3, *p < 0.05, **p < 0.01, ***p < 0.001, ****p < 0.0001).

NIR completely closed on day 14 compared to H-Fe^{2+} of 94.6%, but those in PBS and Tegaderm were still as high as 19.3% and 14.3%, respectively. These results showed that the PGA composite hydrogels could accelerate wound healing with the assistance of mild photothermal stimulation, during which both Zn^{2+}@TA and Fe^{2+}@TA cooperatively pro-healed the wound process.

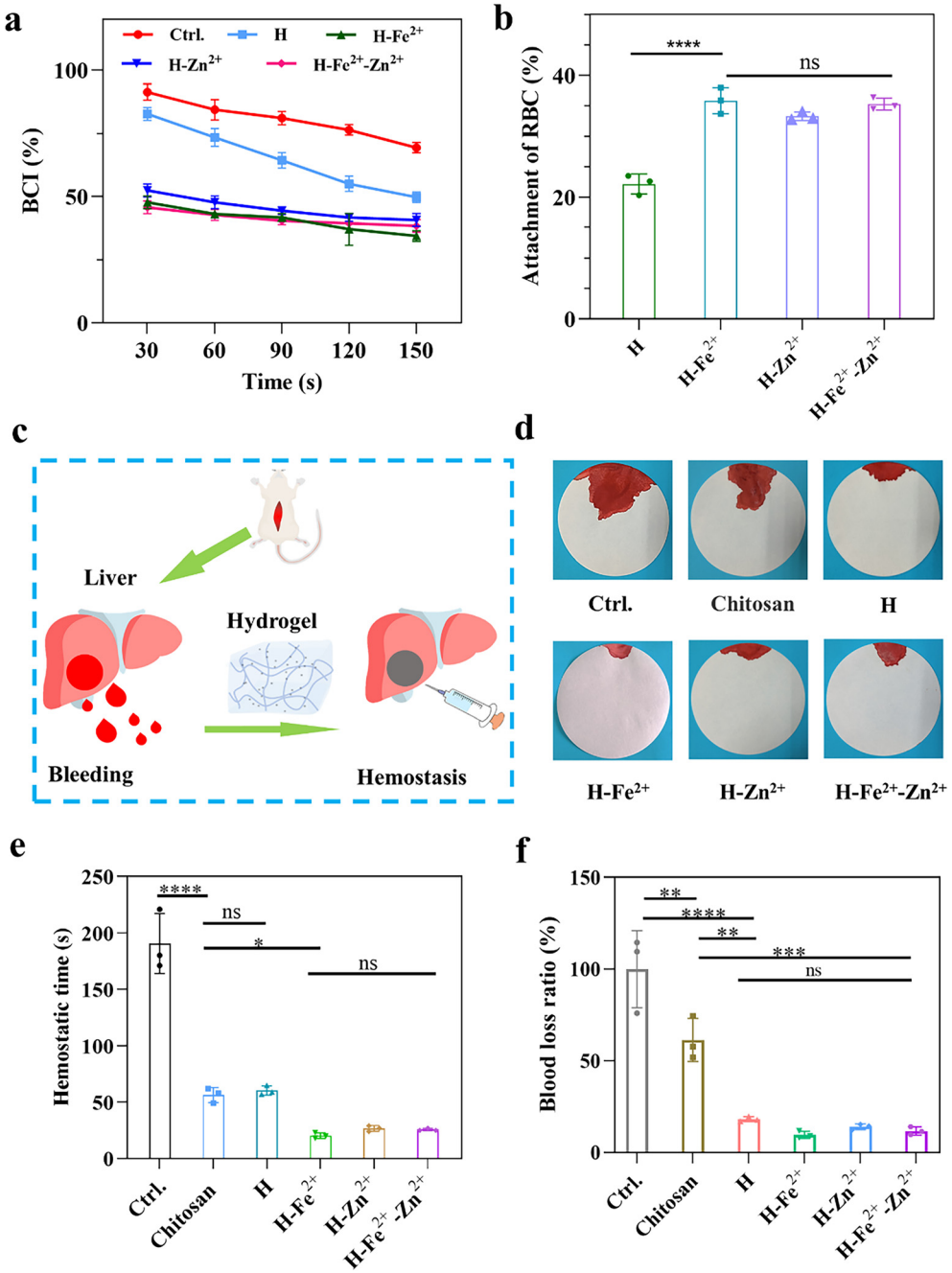

Fig. 5 Hemostatic performance evaluation of the PGA composite hydrogels. (a) Blood coagulation index (BCI); (b) the adsorption of red blood cells (RBC); (c) schematic diagram of the rat liver bleeding model; (d) representative photos of bleeding experiments; (e) hemostasis time; and (f) blood loss ratio in the rat liver hemostasis model (n = 3, *p < 0.05, **p < 0.01, ***p < 0.001, ****p < 0.0001).

H&E staining is a commonly used technique and was used for observing the regenerated tissues on days 3, 7, and 14; all groups presented a time-dependent inflammation relief as a typical healing process (Fig. 7a). Compared to the high levels of inflammatory cells observed in PBS, Tegaderm, H and H-Fe^{2+} (Fig. S15†), H-Zn^{2+}, H-Fe^{2+}-Zn^{2+}, H-Fe^{2+}-NIR, and H-Fe^{2+}-Zn^{2+}-NIR reduced the inflammation response heavily, indicating that both Zn^{2+} and mild photothermal stimulation could relieve the inflammation.[55] On the 14th day, inflammation was the weakest in H-Fe^{2+}-Zn^{2+} (12.6%) and H-Fe^{2+}-Zn^{2+}-NIR (10.3%). These results indicate that the PGA composite hydrogels can greatly relieve wound inflammation through the cooperative effect of metal-ions@TA nanoparticles and mild photothermia, accelerating the transition from inflammation to proliferation.

During the late stage of wound healing, granulation growth and re-epithelialization are considered to be key steps following dermis regeneration, which provides early reconstruction

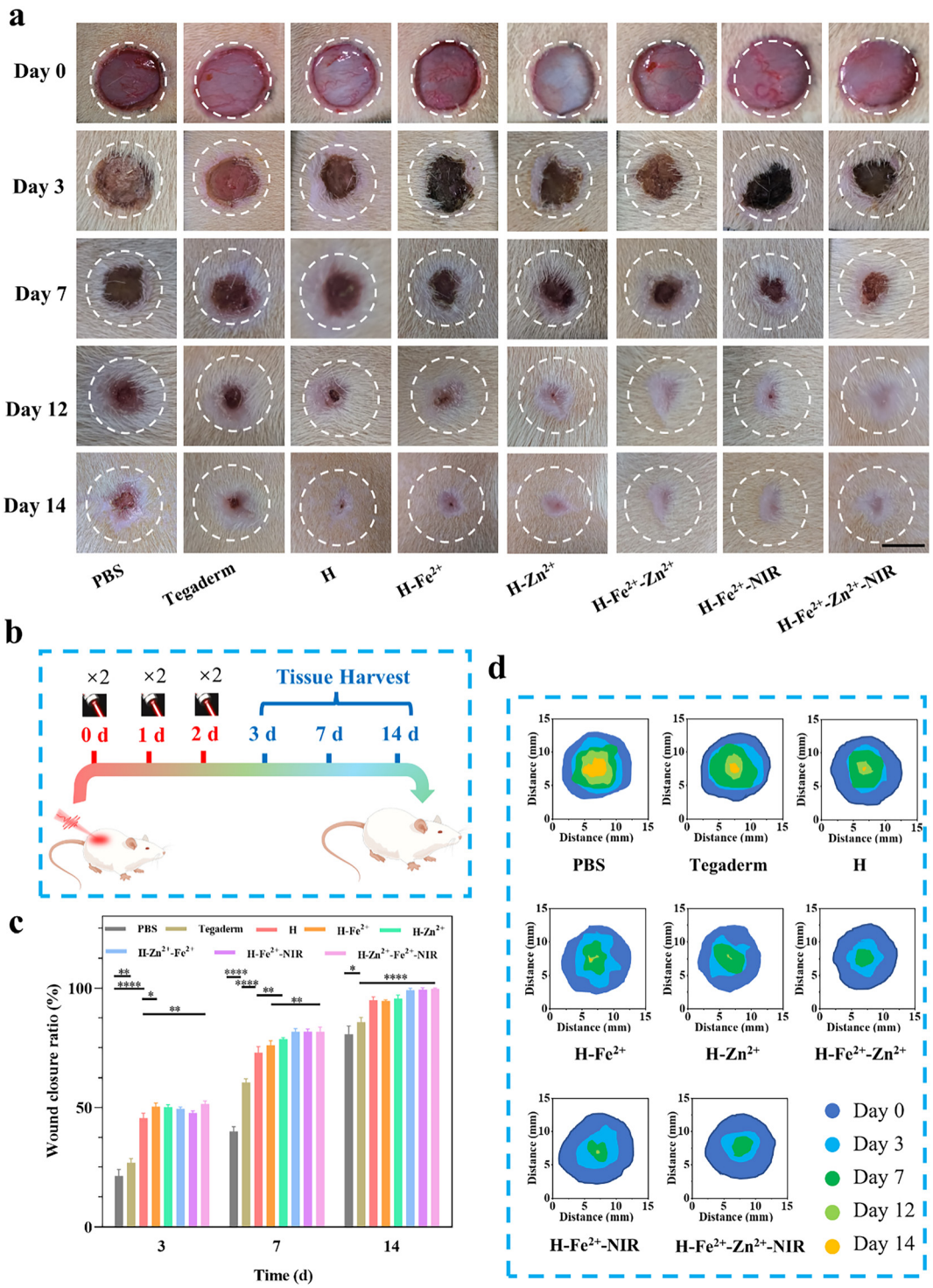

Fig. 6 The full-thickness rat-skin defect model to evaluate wound healing. (a) Representative photos of wounds over the treatment time; (b) schematic diagram for the process of wound treatment; (c) wound closure ratio over the treatment time; and (d) the diagrams of time-evolved wound areas (n = 3, scale bar = 5 mm, *p < 0.05, **p < 0.01, ***p < 0.001, ****p < 0.0001).

of functional barriers for preventing *trans*-epidermal water loss and infections.[56] Obviously, the tissue sections of the healed wounds in H-Fe^{2+}-Zn^{2+}, H-Fe^{2+}-NIR, and H-Fe^{2+}-Zn^{2+}-NIR showed relatively complete epithelium compared to PBS and Tegaderm on day 14. Moreover, on the 14th day, the granulation tissues in all hydrogel groups tended to convert mainly into epidermis and dermis, except PBS and Tegaderm, suggesting that the wounds also did not undergo disorderly proliferation (Fig. 7b and Fig. S16†).[57] Furthermore, the regenerated hair follicles are important indicators to evaluate high-

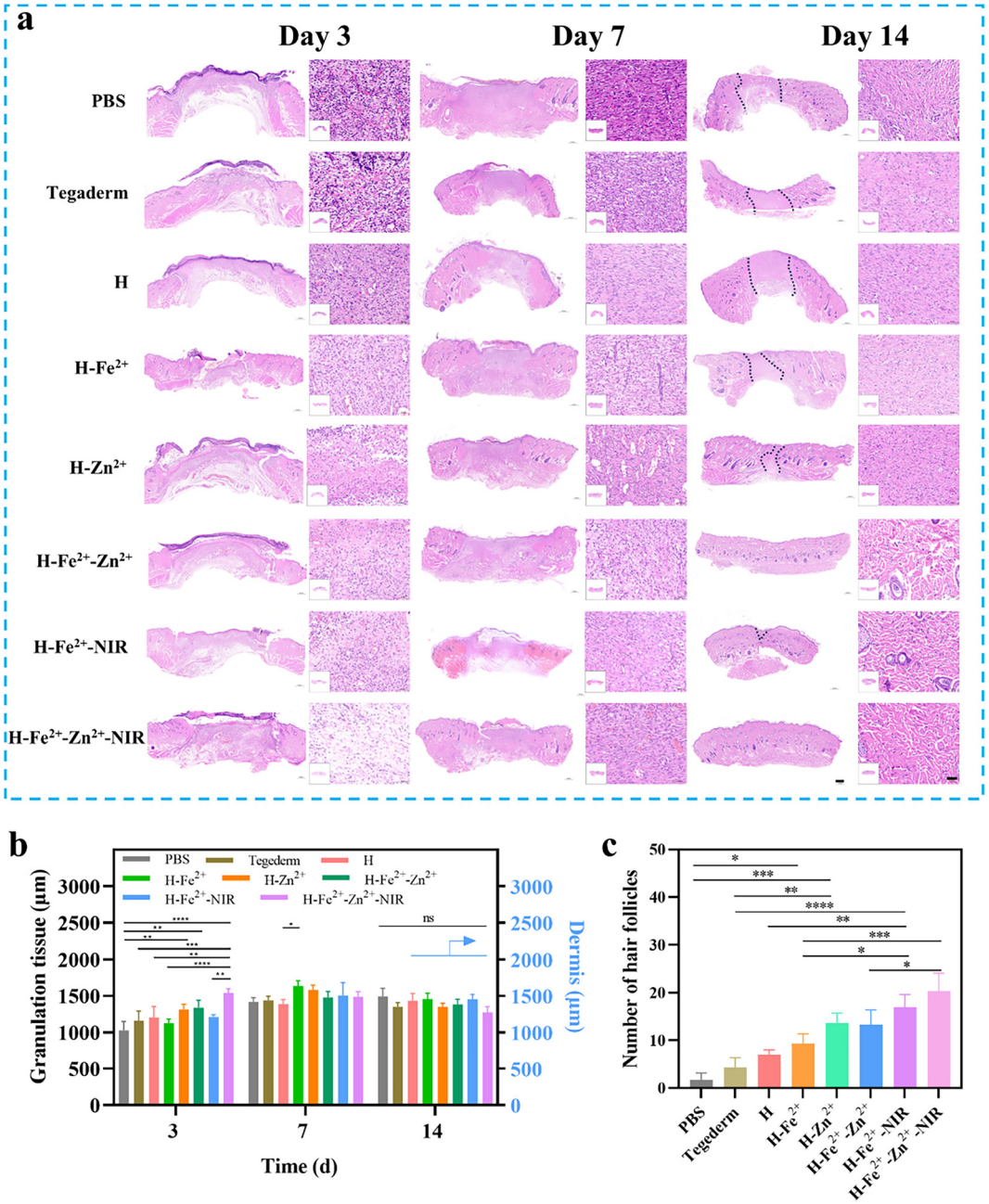

Fig. 7 (a) Representative H&E staining images of wound regeneration tissue (the dot line denotes the wound gap; scale bar in full image = 500 μm, scale bar in enlarged image = 50 μm); (b) granular tissue and dermis thickness; (c) the number of regenerated hair follicles (n = 3, *p < 0.05, **p < 0.01, ***p < 0.001, ****p < 0.0001).

quality skin healing.[58] As shown in Fig. 7c, H-Fe^{2+}-NIR and H-Fe^{2+}-Zn^{2+}-NIR regenerated more hair follicles, further providing evidence that both metal-ions@TA and mild photothermia cooperatively promoted the high-quality healing process.

2.8 *In vivo* macrophage polarization from M1 to M2

Macrophages are key participants in the local immune microenvironment of wounds to promote tissue repair, angiogenesis, and secretion of the extracellular matrix.[59,60] In particular, the regulation of macrophages from pro-inflammatory M1 to anti-inflammatory or pro-healing M2 is a key step in accelerating wound healing; otherwise, acute wounds would transform into chronic wounds.[61] Therefore, immunofluorescence staining was performed to assess the levels of inflammation on days 3 and 7, in which CD86 and CD206, respectively, identified M1 and M2 (Fig. 8a and b). All the hydrogels reduced the proportion of M1 but increased that of M2 in wounds over the treatment time, and the effect is especially amplified in H-Zn^{2+}, H-Fe^{2+}-Zn^{2+}, and H-Fe^{2+}-Zn^{2+}-NIR (Fig. 8d, e and Table S2†). These data indicate that Zn^{2+}@TA

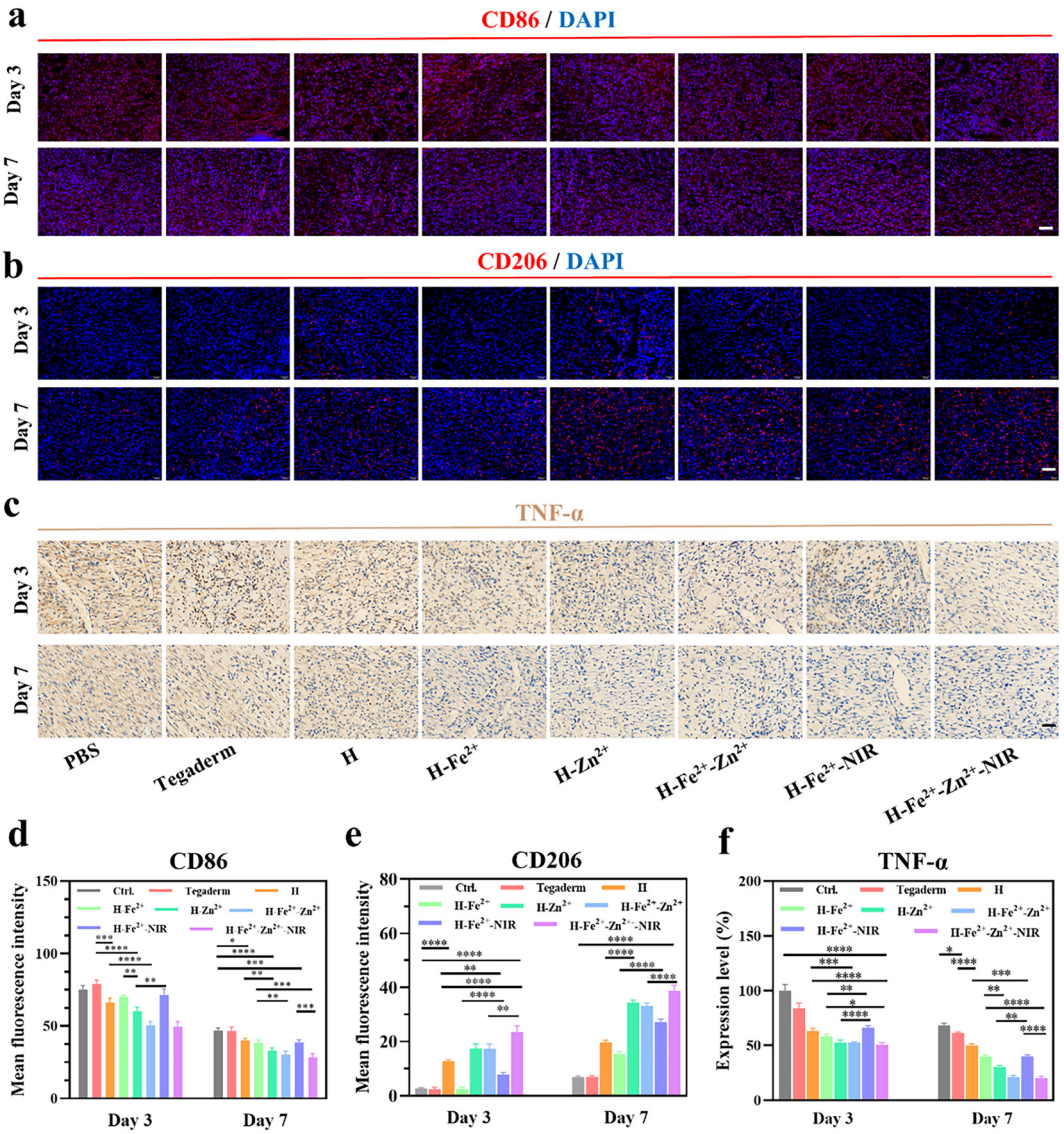

Fig. 8 Histological evaluation of wound inflammation and macrophage polarization phase. Representative (a) CD86 (red area) and (b) CD206 (red area) immunofluorescence staining images of wound tissues on days 3 and 7; (c) representative TNF-α immunohistochemical staining images (brown area denotes inflammation), mean fluorescence intensity of (d) CD86, (e) CD206, and (f) expression level of TNF-α (n = 3, scale bar = 50 μm, *p < 0.05, **p < 0.01, ***p < 0.001, ****p < 0.0001).

played a major role in reshaping the pro-healing wound microenvironment, besides an auxiliary effect of mild photothermia, which is consistent with *in vitro* macrophage polarization.[62,63] In addition, TNF-α signifies the intensity of the inflammatory response in wounds, and immunohistochemical staining was performed to assess the levels of TNF-α in the regenerated tissues (Fig. 8c). Fig. 8f shows that the level of TNF-α was significantly lower on day 7 than on day 3. Specifically, the inflammatory response in H-Zn^{2+}, H-Fe^{2+}-Zn^{2+}, and H-Fe^{2+}-Zn^{2+}-NIR was relieved more than that in Tegaderm and others. These data provide evidence that Zn^{2+}@TA played a major role in effectively reducing the inflammation, which is consistent with the above CD86/CD206 staining. Collectively, the immunofluorescence and immunohistochemical analyses demonstrate that the PGA composite hydrogels could regulate pro-inflammatory M1 to pro-healing M2 and shorten the inflammation period to accelerate wound healing, which was boosted in the treatments of H-Zn^{2+}, H-Fe^{2+}-Zn^{2+}, and H-Fe^{2+}-Zn^{2+}-NIR.

2.9 *In vivo* neovascularization and collagen deposition

A hallmark of the proliferative stage of wound healing is strong angiogenesis. Blood vessels transport oxygen, nutrients, and cytokines to reach wounds and maintain the growth of regenerative tissue.[64] Meanwhile, healthy vascularized granulations provide support for the growth and migration of keratinocytes to initiate epithelial regeneration.[37] CD31, also known as platelet endothelial cell adhesion molecule, is commonly used to indicate the formation of new blood vessels, and

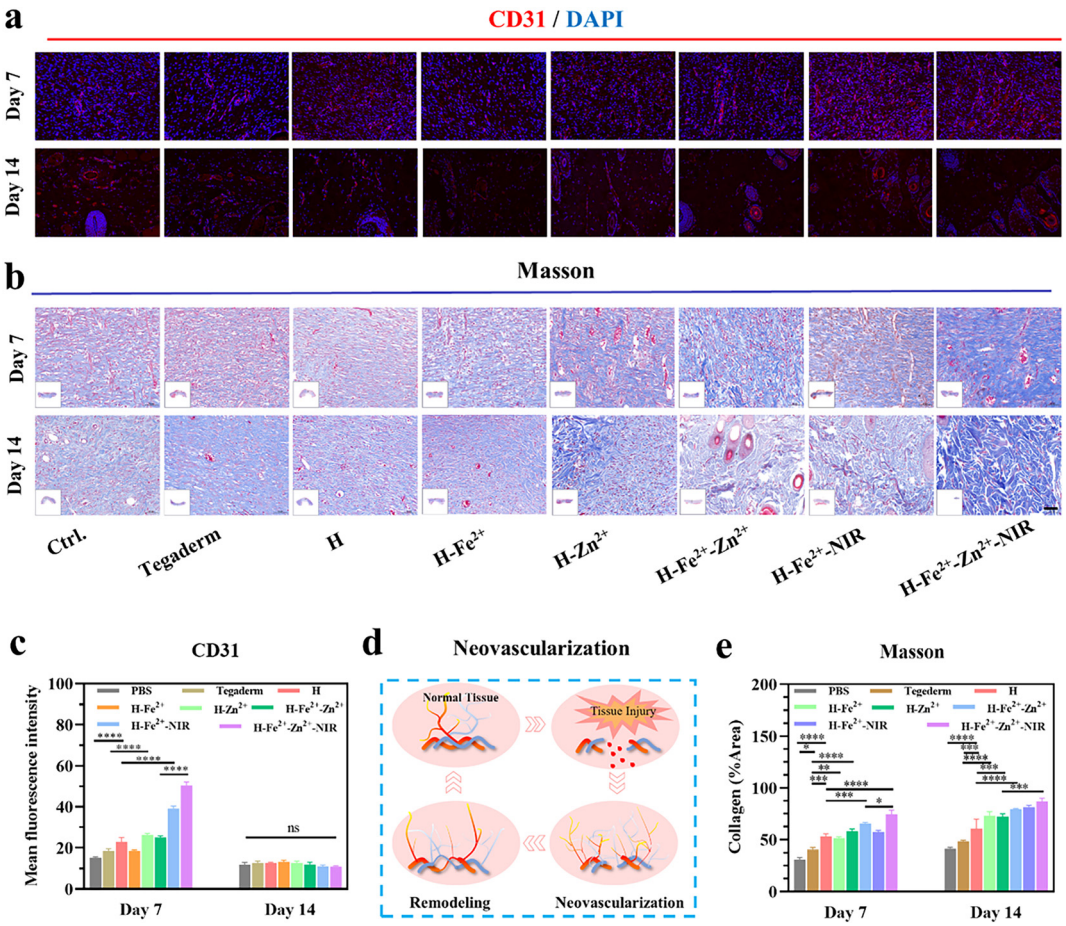

Fig. 9 Histological evaluation of the wound remodeling phase. (a) Representative immunofluorescence staining images of CD31 (red area) on days 7 and 14; (b) representative images of Masson staining on days 7 and 14; (c) CD31 relative level; (d) schematic diagram of neovascularization; (e) collagen deposition levels of the regenerated tissues (n = 3, scale bar = 50 μm, *p < 0.05, **p < 0.01, ***p < 0.001, ****p < 0.0001).

CD31-labeled immunofluorescence staining was used to observe the healed tissues on the 7th and 14th days (Fig. 9a and Table S2†). The red fluorescence intensity is positively correlated with the formation of new blood vessels. As shown in Fig. 9c and d, the wounds treated with H-Zn^{2+}, H-Fe^{2+}-Zn^{2+}, H-Fe^{2+}-NIR, and H-Fe^{2+}-Zn^{2+}-NIR showed higher levels of CD31 than H-Fe^{2+}, H, and Tegaderm on day 7, which indicates that Zn^{2+}@TA and mild photothermia mainly stimulated angiogenesis.[11] It is clear that the number of blood vessels decreased on day 14 compared to that on day 7, but the morphology of blood vessels changed from slender capillaries to thicker ones. Based on the angiogenesis pattern during wound healing, this result indicates a normal transition from proliferation to remodeling. Moreover, collagen is the protein with the highest content in skin, and collagen deposition signifies the degree of wound healing and the integrity of regenerated skin. Blue collagen fibers, red muscle fibers, and blue-black nuclei were shown in the Masson trichrome staining of the tissue sections (Fig. 9b). On days 7 and 14, the levels of collagen deposition in all hydrogels were higher than Tegaderm, and the composite hydrogels performed better than pure H; remarkably, H-Fe^{2+}-Zn^{2+}-NIR showed denser networks with regular orientation on day 14 (Fig. 9e). These data further demonstrate that the PGA composite hydrogels can accelerate collagen deposition to remodel the regenerated tissues *via* the cooperative effect of metal-ions@TA and mild photothermia. In all, the above CD31 immunofluorescence staining and Masson trichrome staining demonstrate that the PGA composite hydrogels could promote neovascularization and collagen deposition *via* cooperative metal-ions@TA nanoparticle and mild photothermal stimulation.

3 Conclusion

In summary, we facilely constructed a type of wound microenvironment regulatory polypeptide PGA composite hydrogel containing metal ion-coordinated nanoparticles, which exhibit NIR-mediated photothermia, ROS clearance, and multiple wound pro-healing activities. *In vitro* and *in vivo* assays provide evidence that the PGA composite hydrogels plus mild photothermia could not only promote cell proliferation, migration, and angiogenesis, but also alleviate inflammation and polarize pro-inflammatory M1 macrophages into pro-healing

M2 macrophages, thus effectively accelerating wound healing. These composite hydrogels could greatly reduce the blood loss ratio to about 10% and stop rat liver bleeding for about 25 s compared to commercial chitosan-based hemostats. Remarkably, the full-thickness skin defect models illustrate that the composite hydrogels of H-Fe^{2+}-Zn^{2+} plus mild photothermia achieved optimal wound healing with a fast rate, a thick regenerated dermis/epidermis, more hair follicles, and a high level of collagen deposition compared to Tegaderm. Consequently, this work provides a versatile platform to construct the polypeptide PGA composite hydrogels that hold promising as potent wound dressings and hemostats.

4 Experimental section

4.1 Preparation of the PGA composite hydrogel

According to our previous method,[4] the lyophilized dopamine-modified PGA (1.0 wt%) that was treated by an "oxidation–lyophilization" method was added to PBS (pH 7.4) or the solution of 0.1 wt% metal ion-coordinated nanoparticles to prepare the corresponding hydrogels, which were named H (pure PGA hydrogel), H-Fe^{2+} (H with Fe^{2+}@TA), H-Zn^{2+} (H with Zn^{2+}@TA), and H-Fe^{2+}-Zn^{2+} (H with Fe^{2+}-Zn^{2+}@TA), respectively, and then used immediately.

4.2 DPPH radical scavenging assay

The antioxidant properties of hydrogels were evaluated *via* a DPPH radical scavenging assay.[10] Briefly, 1.5 mM DPPH solution was prepared in anhydrous ethanol and stored in the dark. Then, 200 μL of dDPPH solution and 2.8 mL of ethanol were added into 200 μL of H, H-Fe^{2+}, H-Zn^{2+}, and H-Fe^{2+}-Zn^{2+} hydrogels, respectively. Then, the samples were incubated in the dark at 37 °C for 30 min. The mixture of DPPH solution (200 μL), PBS solution (200 μL), and ethanol (2.8 mL) obtained using the same treatment was used as a control sample. The absorbance of the supernatant was recorded at 517 nm, and each group of samples was repeated three times. The percentage of DPPH scavenging was calculated according to the following formula:

$$\text{DPPH scavenging ratio } (\%) = (\text{OD}_{\text{control}} - \text{OD}_{\text{sample}})/\text{OD}_{\text{control}} \times 100$$

4.3 *In vitro* cytocompatibility

In vitro cytocompatibility of the hydrogels was characterized by a common MTT method and live/dead cell double staining. For MTT, 100 μL of hydrogel was prepared in 96-well plates, washed three times with PBS solution after 10 min of incubation, and sterilized with a 254 nm ultraviolet lamp for 15 min. Then, L929 fibroblasts (100 μL, 1×10^4 cells per well) were planted on the surface of the hydrogel and cultured in a culture incubator (5% CO_2, 37 °C) for 24 h, respectively. Subsequently, the cells were rinsed with PBS solution, and 100 μL of MTT solution was added to each well and incubated for 4 h. The optical density (OD) at 490 nm was measured with a microplate reader (Thermo Scientific Varioskan LUX). All samples were repeated five times ($n = 5$). For the live/dead cell double staining experiment, 200 μL of hydrogel was prepared at the bottom of 24-well plates and sterilized by ultraviolet irradiation for 15 min. Then, L929 fibroblasts (1×10^5 cells per well) were cultured with hydrogel for 24 h. Finally, the cells were stained with a live/dead cell double staining kit and photographed using an inverted fluorescence microscope (Olympus IX73).

4.4 *In vitro* cell migration

The scratch experiment of L929 cells was used to assess *in vitro* migration. To ensure that cell migration was not caused by cell proliferation, L929 cells were starved with low serum-containing culture medium for 24 h before construction of the scratch according to a previous protocol.[35] A scratch was created in each well with a 100-μL pipette after the cells were seeded into a 6-well plate and cultured to 80% density. Then the cells were cultured with fresh culture medium containing 1% FBS and cultured with different samples for 24 h and 48 h, followed by mild photothermal stimulation at about 40–42 °C (808 nm, 10 min, 1 W cm^{-2}). Finally, the cell migration was photographed using an Olympus IX73 microscope.

4.5 Measurement of intracellular ROS scavenging ability

After the L929 cells were inoculated on 12-well plates (1×10^5 cells per well), a DCFH-DA probe was utilized to assess the ROS scavenging ability. First, 100 μM H_2O_2 was added to stimulate cells to produce ROS, and each hydrogel sample (H, H-Fe^{2+}, H-Zn^{2+}, and H-Fe^{2+}-Zn^{2+}) was added for incubation. The DACH-DA probe was added after 4 h, incubated for 20 min, and photographed by an Olympus IX73 microscope.

4.6 Tube formation assessment

First, 100 μL of pre-chilled Matrigel was spread in 24-well plates and formed into gel at 37 °C for 30 min.[65] Then HUVECs were seeded in a 24-well plate at a density of 3×10^4 cells per well and cultured with different hydrogels (H, H-Fe^{2+}, H-Zn^{2+}, and H-Fe^{2+}-Zn^{2+}) after 6 h. Finally, the bright field pictures were taken by an Olympus IX73 microscope and evaluated using ImageJ software (NIH, ImageJ 1.8, USA).

4.7 CD86 and CD206 immunofluorescence staining

RAW 264.7 were incubated on 6-well plates, co-incubated with different hydrogel samples (H, H-Fe^{2+}, H-Zn^{2+}, and H-Fe^{2+}-Zn^{2+}), and stimulated with 100 ng mL^{-1} LPS.[19] The cells were fixed in 4% paraformaldehyde for 30 min, permeabilized with 0.2% Triton X-100 for 10 min, and blocked with 10% BSA for 30 min. The primary antibody CD86 was added, and the cells were incubated overnight at 4 °C. Next, the cells were incubated with Alexa Fluor 488-conjugated AffiniPure goat anti-rabbit IgG (H + L) for 1 h at 37 °C. Finally, the cells were stained with DAPI for 10 min and observed by an Olympus IX73 microscope. CD206 immunofluorescence staining was performed following the same steps.

4.8 qRT-PCR analysis

Raw 264.7 cells were inoculated on 6-well plates, stimulated with 100 ng mL^{-1} LPS, and then cultured with different hydrogel samples (H, H-Fe^{2+}, H-Zn^{2+}, and H-Fe^{2+}-Zn^{2+}).[19] Total RNA was extracted through an EZ-press RNA Purification Kit and reverse-transcribed to cDNA by Prime Script™ RT Master Mix after 24 h of incubation. SYBR Green qPCR Master Mix was used to perform RT-PCR on a Quant Studio™ 6 Flex Allegra X-30 (Thermo Scientific), and glyceraldehyde-3-phosphate dehydrogenase (GAPDH) was used to normalize the data. qRT-PCR-related primer sequences are shown in Table S3.†

4.9 *In vivo* animal study

All animal procedures were performed in accordance with the Guidelines for Care and Use of Laboratory Animals of "Shanghai Jiao Tong University" and approved by the Animal Ethics Committee of "Shanghai Jiao Tong University." SD rats (male, 200–250 g) were purchased from Shanghai Slac (China).

4.10 *In vivo* biocompatibility

First, 200 μL of hydrogel was subcutaneously implanted in the backs of SD rats (n = 3). Then, the residual hydrogels and their surrounding tissues were taken out after implantation for 7 and 14 days. Hematoxylin–eosin (H&E) staining was employed and observed with an Olympus BX53 microscope.

4.11 *In vivo* hemostatic capability

The SD rats were exposed to the liver after being anesthetized with isoflurane and placing the leaf on filter paper. An incision with a diameter of 5 mm was then created on the surface of the liver. The hydrogel (H, H-Fe^{2+}, H-Zn^{2+}, and H-Fe^{2+}-Zn^{2+}) was injected into the bleeding sites. Finally, the filter paper was weighed after 2 min to measure the blood loss, and the bleeding time was recorded. Wounds without any treatment are regarded as a negative control, and commercial chitosan dressing is regarded as a positive control. The relative blood loss amount was calculated using the following equation:

$$\text{Relative blood loss } \% = M_{\text{sample}}/M_{\text{negative}} \times 100.$$

4.12 *In vivo* wound healing performance

The full-thickness skin defect model of SD rats was constructed to evaluate wound healing, and 1 cm-diameter wounds in the back of rats were created using surgical scissors. All mice were randomly divided into 8 groups: PBS, Tegaderm, H, H-Fe^{2+}, H-Zn^{2+}, H-Fe^{2+}-Zn^{2+}, H-Fe^{2+}-NIR, and H-Fe^{2+}-Zn^{2+}-NIR. The control groups were treated with PBS or Tegaderm™ film, respectively. The hydrogel groups were treated with H, H-Fe^{2+}, H-Zn^{2+} and H-Fe^{2+}-Zn^{2+}, H-Fe^{2+}-NIR, H-Fe^{2+}-Zn^{2+}-NIR (NIR denotes the irradiation of 808 nm, 1 W cm^{-2}, 10 min). The wound healing process was recorded, and the wound area was measured using Image J software. The wound healing ratio was calculated using the following formula:

$$\text{Wound healing ratio } (\%) = (S_0 - S_t)/S_0 \times 100,$$

where S_0 and S_t represent the area at time = 0 or t. Samples collected on days 3, 7, and 14 were fixed with 4% paraformaldehyde, embedded in paraffin, and cut into sections. Samples collected on days 3, 7, and 14 were used for H&E staining to analyze the thickness of granulation or dermal tissues, inflammatory cells, and hair follicles. The samples collected on days 7 and 14 were also used for Masson's trichrome to assess the collagen deposition in regenerated tissues. In addition, immunohistochemical staining of TNF-α and immunofluorescence staining of CD86, CD206, and CD31 were conducted to evaluate tissue inflammation, macrophage polarization, and vascular regeneration. The images were taken with a microscope (Olympus VS200, Japan) and analyzed using Image J software.

4.13 Statistical analysis

Statistical data are given as the mean ± standard deviation, and statistical significance was obtained by a one-way or two-way ANOVA, followed by Tukey's honestly significant difference (HSD); the p value was output in GraphPad (GP) style. *p < 0.05, **p < 0.01, ***p < 0.001, and ****p < 0.0001 represent a sequential increase in statistical significance, and *p < 0.05 is considered statistically significant.

Conflicts of interest

These authors declare no competing financial interest.

Author contributions

C. M. Dong conceived the study, designed strategies, discussed results, supervised the project, and wrote and finalized the paper. C. Du supervised biological experiments. Y. Z. Chen performed all experiments, analyzed the data, and wrote the article. X. L. Zhang assisted in some animal experiments. Q. Wang performed some biological experiments. All the authors discussed and contributed to the final manuscript.

Acknowledgements

C.-M. Dong acknowledges the financial support provided by the National Natural Science Foundation of China (22375125; 22075176) and the Shanghai Natural Science Fund (22ZR1429200). C. Du acknowledges the financial support provided by the Shanghai Sailing Program (22YF1445500).

References

1 B. L. Guo, R. N. Dong, Y. P. Bang and M. Li, *Nat. Rev. Chem.*, 2021, **5**, 773–791.
2 T. A. Harris-Tryon and E. A. Grice, *Science*, 2022, **376**, 940–945.

3 M. Kharaziha, A. Baidya and N. Annabi, *Adv. Mater.*, 2021, **33**, 2100176.
4 P. S. Briquez, L. E. Clegg, M. M. Martino, F. M. Gabhann and J. A. Hubbell, *Nat. Rev. Mater.*, 2016, **1**, 15006.
5 A. S. Kimball, F. M. Davis, A. denDekker, A. D. Joshi, M. A. Schaller, J. Bermick, X. Xing, C. F. Burant, A. T. Obi, D. Nysz, S. Robinson, R. Allen, N. W. Lukacs, P. K. Henke, J. E. Gudjonsson, B. B. Moore, S. L. Kunkel and K. A. Gallagher, *Immunity*, 2019, **51**, 258–271.
6 M. Kloc, R. M. Ghobrial, J. Wosik, A. Lewicka, S. Lewicki and J. Z. Kubiak, *J. Tissue Eng. Regener. Med.*, 2019, **13**, 99–109.
7 Z. D. Xia, A. Sato, M. A. Hughes and G. W. Cherry, *Wound Repair Regen.*, 2000, **8**, 138–144.
8 G. Gethin, J. D. Ivory, D. Sezgin, H. Muller, G. O'Connor and A. Vellinga, *Wound Repair Regen.*, 2021, **29**, 843–847.
9 C. Du, L. Zhou, J. Qian, M. He, Z. G. Zhang, C. Feng, Y. Zhang, R. Zhang and C. M. Dong, *ACS Appl. Mater. Interfaces*, 2021, **13**, 44002–44012.
10 L. Teng, Y. Song, L. Hu, Q. Bai, X. Zhang and C.-M. Dong, *Chin. J. Chem.*, 2023, **41**, 2103–2112.
11 L. Sheng, Z. Zhang, Y. Zhang, E. Wang, B. Ma, Q. Xu, L. Ma, M. Zhang, G. Pei and J. Chang, *Biomaterials*, 2021, **264**, 120414.
12 R. Li, K. Liu, X. Huang, D. Li, J. Ding, B. Liu and X. Chen, *Adv. Sci.*, 2022, **9**, 2105152.
13 Y. Liang, J. He and B. Guo, *ACS Nano*, 2021, **15**, 12687–12722.
14 Z. Zhang, C. He and X. Chen, *Adv. Mater.*, 2023, 2308894.
15 Y. Chen, Y. Song, X. Zhu, C.-M. Dong and M. Chen, *Polym. Rev.*, 2023, **2281462**, 1–47.
16 X. Zhou and Z. Li, *Adv. Healthcare Mater.*, 2018, **7**, 1800020.
17 Z. Zou, Z. Zhang, H. Ren, X. Cheng, X. Chen and C. He, *Biomaterials*, 2023, **301**, 122251.
18 Q. Bai, L. Teng, X. Zhang and C. M. Dong, *Adv. Healthcare Mater.*, 2022, **11**, 2101809.
19 Y. N. Qian, Y. J. Zheng, J. Jin, X. Wu, K. J. Xu, M. L. Dai, Q. Niu, H. Zheng, X. J. He and J. L. Shen, *Adv. Mater.*, 2022, **34**, 2200521.
20 Y. Guo, Q. Sun, F.-G. Wu, Y. Dai and X. Chen, *Adv. Mater.*, 2021, **33**, 2007356.
21 J. J. R. H. Ejima, K. Liang, J. P. Best, M. P. van Koeverden, G. K. Such, J. Cui and F. Caruso, *Science*, 2013, **341**, 154–157.
22 Q. Li, X. S. Li, E. Bury, K. Lackey, A. Koh, U. Wesselmann, T. Yaksh and C. Zhao, *Adv. Funct. Mater.*, 2023, **33**, 2301025.
23 Z. Li and K. M. Bratlie, *Macromol. Biosci.*, 2021, **21**, 2100031.
24 M. Chen, T. Chen, J. Bai, S. He, M. Luo, Y. Zeng, W. Peng, Y. Zhao, J. Wang, X. Zhu, W. Zhi, J. Weng, K. Zhang and X. Zhang, *Adv. Healthcare Mater.*, 2023, 2301560.
25 W. Xue, R. Yang, S. Liu, Y. Pu, P. Wang, W. Zhang, X. Tan and B. Chi, *Biomater. Sci.*, 2022, **10**, 2417–2427.
26 Z. He, H. Luo, Z. Wang, D. Chen, Q. Feng and X. Cao, *Carbohydr. Polym.*, 2023, **299**, 120180.
27 Y. Li, R. Fu, Z. Duan, C. Zhu and D. Fan, *Bioact. Mater.*, 2021, **9**, 461–474.
28 K. Yang, S. Zhao, B. Li, B. Wang, M. Lan and X. Song, *Coord. Chem. Rev.*, 2022, **454**, 214330.
29 W. Wang, Y. Gao, W. Xu, Y. Xu, N. Zhou, Y. Li, M. Zhang and B. Z. Tang, *Adv. Mater.*, 2023, 2307785.
30 F. Yang, Y. Xue, F. Wang, D. Guo, Y. He, X. Zhao, F. Yan, Y. Xu, D. Xia and Y. Liu, *Bioact. Mater.*, 2023, **26**, 88–101.
31 J. Tan, S. Li, C. Sun, G. Bao, M. Liu, Z. Jing, H. Fu, Y. Sun, Q. Yang, Y. Zheng, X. Wang and H. Yang, *Adv. Healthcare Mater.*, 2023, 2302305.
32 Y. Liu, A. Suarez-Arnedo, E. L. P. Caston, L. Riley, M. Schneider and T. Segura, *Adv. Mater.*, 2023, 2304049.
33 A. C. Ponsen, R. Proust, S. Soave, F. Mercier-Nome, I. Garcin, L. Combettes, J. J. Lataillade and G. Uzan, *Bioact. Mater.*, 2022, **18**, 368–382.
34 A. A. Solbu, D. Caballero, S. Damigos, S. C. Kundu, R. L. Reis, O. Halaas, A. S. Chahal and B. L. Strand, *Mater. Today Bio*, 2023, **18**, 100537.
35 J. Xiao, S. Chen, J. Yi, H. F. Zhang and G. A. Ameer, *Adv. Funct. Mater.*, 2017, **27**, 1604872.
36 F. Yang, Y. J. Xue, F. L. Wang, D. N. Guo, Y. J. He, X. Zhao, F. Y. Yan, Y. Q. Xu, D. D. Xia and Y. S. Liu, *Bioact. Mater.*, 2023, **26**, 88–101.
37 H. R. Moreira and A. P. Marques, *Curr. Opin. Biotechnol.*, 2022, **73**, 253–262.
38 C. H. Xian, Z. Zhang, X. R. You, Y. F. Fang and J. Wu, *Adv. Funct. Mater.*, 2022, **32**, 2202410.
39 X. Wang, B. Gao, M. Wang, Q. Wang, S. Xia, W. Zhang, X. Meng and Y. Feng, *Chem. Eng. J.*, 2023, **452**, 139670.
40 D. B. Guo, Y. Huang, X. Jin, C. Zhang and X. Y. Zhu, *Biomaterials*, 2021, **266**, 120400.
41 H. Sies and D. P. Jones, *Nat. Rev. Mol. Cell Biol.*, 2020, **21**, 363–383.
42 S. Roy, S. Khanna, K. Nallu, T. K. Hunt and C. K. Sen, *Mol. Ther.*, 2006, **13**, 211–220.
43 M. Hesketh, K. B. Sahin, Z. E. West and R. Z. Murray, *Int. J. Mol. Sci.*, 2017, **18**, 1545.
44 P. J. Murray, *Annu. Rev. Physiol.*, 2017, **79**, 541–566.
45 W. G. Liu, M. Wang, W. Cheng, W. Niu, M. Chen, M. Luo, C. X. Xie, T. T. Leng, L. Zhang and B. Lei, *Bioact. Mater.*, 2021, **6**, 721–728.
46 L. Wang, L. Duan, G. Liu, J. Sun, M.-A. Shahbazi, S. C. Kundu, R. L. Reis, B. Xiao and X. Yang, *Adv. Sci.*, 2023, **10**, 2207352.
47 W. Liu, J. Li, M. Cheng, Q. Wang, K. W. K. Yeung, P. K. Chu and X. Zhang, *Adv. Sci.*, 2018, **5**, 1800749.
48 B. Tao, C. Lin, X. Qin, Y. Yu, A. Guo, K. Li, H. Tian, W. Yi, D. Lei, Y. Chen and L. Chen, *Mater. Today Bio*, 2022, **13**, 100216.
49 X. Sun, P. Jia, H. Zhang, M. Dong, J. Wang, L. Li, T. Bu, X. Wang, L. Wang, Q. Lu and J. Wang, *Adv. Funct. Mater.*, 2022, **32**, 2106572.
50 W. Pan, B. Wu, C. Nie, T. Luo, Z. Song, J. Lv, Y. Tan, C. Liu, M. Zhong, T. Liao, Z. Wang, G. Yi, L. Zhang, X. Liu, B. Li, J. Chen and L. Zheng, *ACS Nano*, 2023, **17**, 11253–11267.

51 C. M. Minutti, J. A. Knipper, J. E. Allen and D. M. W. Zaiss, *Semin. Cell Dev. Biol.*, 2017, **61**, 3–11.
52 H. Ren, Z. Zhang, X. Cheng, Z. Zou, X. Chen and C. He, *Sci. Adv.*, 2023, **9**, adh4327.
53 M. Li, S. Zhu, Qi Feng, Z. Qin, H. Gao and X. Cao, *Chem. Eng. J.*, 2023, **468**, 143758.
54 L. Yan, Z. Cao, L. Ren, T. Zhang, J. Hu, J. Chen, X. Zhang, B. Liu, C. Feng, J. Zhu and B. Geng, *Adv. Healthcare Mater.*, 2023, 2302190.
55 G. C. Gurtner, S. Werner, Y. Barrandon and M. T. Longaker, *Nature*, 2008, **453**, 314–321.
56 X. Zhao, Q. Lang, L. Yildirimer, Z. Y. Lin, W. Cui, N. Annabi, K. W. Ng, M. R. Dokmeci, A. M. Ghaemmaghami and A. Khademhosseini, *Adv. Healthcare Mater.*, 2016, **5**, 108–118.
57 J. Liu, M. Y. Qu, C. R. Wang, Y. M. Xue, H. Huang, Q. M. Chen, W. J. Sun, X. W. Zhou, G. H. Xu and X. Jiang, *Small*, 2022, **18**, 2106172.
58 S. F. Ji, Z. Y. Zhu, X. Y. Sun and X. B. Fu, *Signal Transduction Targeted Ther.*, 2021, **6**, 66.
59 R. Medzhitov, *Nature*, 2008, **454**, 428–435.
60 O. Takeuchi and S. Akira, *Cell*, 2010, **140**, 805–820.
61 M. S. Hu, G. G. Walmsley, L. A. Barnes, K. Weiskopf, R. C. Rennert, D. Duscher, M. Januszyk, Z. N. Maan, W. X. Hong, A. T. M. Cheung, T. Leavitt, C. D. Marshall, R. C. Ransom, S. Malhotra, A. L. Moore, J. Rajadas, H. P. Lorenz, I. L. Weissman, G. C. Gurtner and M. T. Longaker, *JCI Insight*, 2017, **2**, 96260.
62 A. Berger, *Br. Med. J.*, 2002, **325**, 1062.
63 N. Denans, N. T. T. Tran, M. E. Swall, D. C. Diaz, J. Blanck and T. Piotrowski, *Nat. Commun.*, 2022, **13**, 5356.
64 S. H. Jung, B. H. Jang, S. Kwon, S. J. Park, T. E. Park and J. H. Kang, *Adv. Mater.*, 2023, 2211149.
65 K. Wang, R. Dong, J. Tang, H. Li, J. Dang, Z. Zhang, Z. Yu, B. Guo and C. Yi, *Chem. Eng. J.*, 2022, **430**, 132664.